Multi-Wall Carbon Nanotube-Embedded Lithium Cobalt Phosphate Composites with Reduced Resistance for High-Voltage Lithium-Ion Batteries

Tae Kyoung Kim,[1,2] Cyrus S. Rustomji,[1,2] Hyung-Man Cho,[1,2] Dongwon Chun,[1,2] Jae-Young Jung,[1,2] Elizabeth Caldwell,[1,2] Youngjin Kim,[1,2] Jun Hyun Han,[1,2,3] and Sungho Jin[1,2,*]

[1]Materials Science & Engineering, and [2]Mechanical and Aerospace Engineering,
University of California at San Diego, 9500 Gilman Dr., La Jolla, CA 92093, USA
[3]Materials Engineering, Chungnam National University, Daejeon 305-764, Korea

Lithium cobalt phosphate (LCP) is a high-voltage cathode material used in high-energy-density lithium-ion batteries. With a novel composite synthesis method, multi-wall carbon nanotube (MWCNT)-embedded LCP nanocomposites (LCP-CNT composites) are synthesized to enhance the electrical conductance of LCP particles, reducing charge-transfer resistance. The LCP-CNT composites with enhanced electrical conductance approximately doubled cell capacity compared to a cell with a bare LCP cathode. The crystal structure of LCP-CNT composite particles is characterized by X-ray diffraction; the microstructures of the embedded MWCNTs inside LCP particles are confirmed by transmission and scanning electron microscopy with focused ion beam procedures. Electrochemical impedance spectroscopy shows the charge-transfer resistance of the cell with the LCP-CNT composite (1.0 wt. % CNT) cathode decreases to ~80 Ω, much smaller than the ~150 Ω charge-transfer resistance of the bare-LCP cathode cell. Based on battery test and impedance analysis, the main factors affecting the capacity increment are the reduced charge transfer resistance and the uniform distribution of MWCNTs, which is formed during the gelation step of the LCP synthesis procedure.

Keywords: lithium cobalt phosphate, carbon nanotube, embedded structure, nano-composite, charge transfer resistance, lithium-ion battery
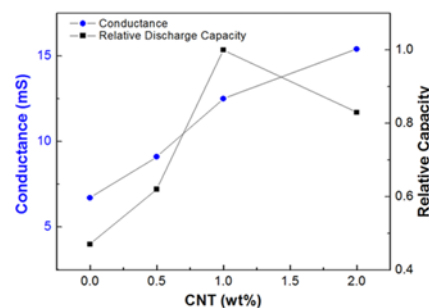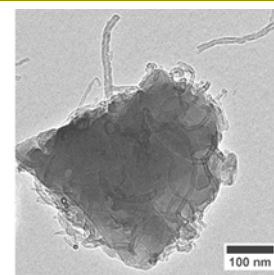
1. INTRODUCTION

The development of high-energy-density lithium-ion batteries (LIBs) is necessary for applications as energy storage systems, which will expand the renewable power plants, decrease oil dependency in vehicles, and reduce the greenhouse gases emitted from conventional hydrocarbon-fueled vehicles.[1-6] Compared to nickel metal hydride batteries with practical energy density of 50 - 100 Wh/kg, LIBs have practical energy density of 80 - 150 Wh/kg, depending on the cathode material, which determines the

capacity and operating voltage.[1,2] Cathode materials for LIBs include layer-structured $LiCoO_2$ (LCO), spinel-structured $LiMn_2O_4$ (LMO), and olivine-structured $LiCoPO_4$ (LCP).[7,8] LCP has an orthorhombic crystal system composed of tetrahedron of P-O bonding and octahedron of Co-O bonding through which Li^+ diffuses one-dimensionally.[9-11] In LMO, and LCO, Li^+ diffuse three- and two-dimensionally, respectively.[8] Although the one-dimensional diffusion of Li^+ in LCP slows charge-transfer reactions, many researchers have studied LCP cathodes because they have high discharge voltages of 4.6 - 4.8 V (vs. Li) and large theoretical capacities of ~167 mAh/g, permitting high specific energy densities of ~800 Wh/kg, compared to the ~400 - 500 and 450 - 550 Wh/kg specific energy densities of LCO and LMO cathodes,

respectively.[12-14]

Despite the advantage of high energy density, LCP cathodes have not been commercialized because of the poor cycle life and capacities experimentally lower than the theoretical values. These drawbacks may result from the low electrical conductivity of ~10^{-15} S/cm, much lower than the ~10^{-9} S/cm conductivity of olivine-structured LiFePO$_4$ (LFP)[15-17] as well as that of conventional LCO (~10^{-3} S/cm).[18] The low electrical conductivities of olivine-structured materials results from the wide band gaps of ~3.7 and 4.4 eV for LFP and LCP, respectively[15,19,20] compared to the ~2.7 eV band gap of LCO.[21] Wide band gaps can slow charge-transfer reactions by the intercalation/de-intercalation of Li$^+$ beyond the point of usability for rechargeable batteries.

Carbon nanotubes (CNTs) are known for excellent physical and mechanical properties, which can be applied in electronic devices, semiconductors, and nanocomposite materials.[12,22-24] CNTs have electrical conductivities of 10^2 - 10^5 S/cm exceeding those of carbon black and graphite;[25,26] thus, CNTs may improve electron mobility within LCP particles when embedded in LCP particles. Many researchers have attempted to improve the cycle life and actual capacity of battery cells with LCP cathodes.[27-29] In one reported study, bare LCP particles deposited onto nonwoven carbon nanofiber webs retained large charge transfer resistances of ~150 Ω in impedance measurements,[29] which may have resulted from the post-mixing of LCP particles with the carbon nanofibers only at the surfaces of the LCP particles.

In this study, multi-wall CNTs (MWCNTs) are embedded in LCP particles, forming LCP-CNT nanocomposites, by dispersing MWCNTs during the gelation between LCP precursors. This method both decreases the charge transfer resistance and distributes the MWCNTs uniformly within the LCP particle. The characterization of CNTs, synthesized bare LCP particles, and the LCP-CNT nanocomposite particles are performed through observation with a focused ion beam (FIB)-scanning electron microscope (SEM). The electrochemical effects of embedding the MWCNTs in LCP particles are analyzed with galvanostatic battery tests, cyclic voltammetry (CV), and electrochemical impedance spectroscopy (EIS) measurements.

2. EXPERIMENTAL PROCEDURE

2.1 Preparation of materials

To fabricate CNT-embedded LCP particles, MWCNTs were dispersed during the gelation of three LCP precursors of LiCl, Co(Ac)$_2$·4H$_2$O, and (NH$_4$)$_2$HPO$_4$ in a stoichiometric ratio, as shown in Fig. 1. The three precursors and MWCNTs were mixed by a slow ball-mixer with yttria-stabilized zirconia balls. After dry mixing, the MWCNT-containing powders were mixed with a small amount of de-ionized (DI) water until gelation occurred, as displayed in Fig. 1. After gelation, mixing and dispersion continued for 2 h to improve the uniformity of the MWCNT distribution within the viscous gel formed by LCP precursors reacting with water.
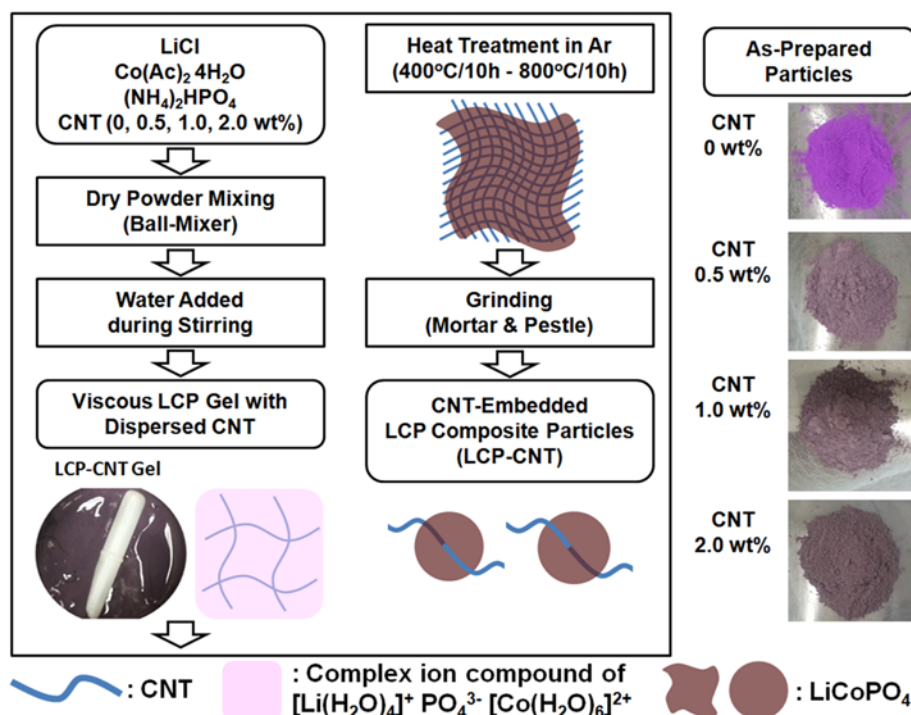

Fig. 1. Synthesis procedure of MWCNT-embedded LCP nanocomposite particles using modified sol-gel method.

Gelation may have result from the formation of the $[Li(H_2O)_4]^+PO_4^{3-}[Co(H_2O)_6]^{2+}$ complex ion compound when DI water was added to the mixture of precursors. In the presence of water, LiCl, Co(Ac)$_2$·4H$_2$O, and (NH$_4$)$_2$HPO$_4$ can form $[Li(H_2O)_4]^+$ cations, $[Co(H_2O)_6]^{2+}$ cations, and PO_4^{3-} anions, respectively. The gel slurry containing the dispersed MWCNTs was poured into an alumina crucible, which was placed in a tube furnace. The tube was purged with Ar gas for 2 h at room temperature (RT), and then heat-treatment was performed under Ar gas with the following temperature profile: RT → holding at 400°C for 10 h → holding at 800°C for 10 h → air-cooling to RT in which a ramping rate was 5°C/min. After heat-treatment, LCP-CNT composite particles were obtained by grinding the heat-treated composites with a mortar and pestle. Optical photos on the right side of Fig. 1 show the synthesized bare LCP and CNT-embedded LCP particles with different CNT amounts. The bare LCP particles are pink in color, while the LCP-CNT composite particles become increasingly dark with increasing the dispersed CNT content.

2.2 Electrode and coin cell fabrication

Coating slurries for the fabrication of cathodes were prepared by mixing bare LCP particles or LCP-CNT composite particles, carbon black, and polyvinylidene fluoride (PVdF) binder in the weight ratio of 8/1/1 (LCP/carbon black/binder) in N-Methyl-2-pyrrolidone solvent. After mixing the slurry for 24 h, the slurry was coated on Al foil of 15 μm thickness with a wire-wound rod (Meyer bar, #60, Gardner Company), then dried at 100°C for 12 h in a vacuum oven. The resulting bare LCP cathode and LCP-CNT composite cathodes had coating layers of ~25 μm thicknesses. For comparison, a simple mixed cathode of bare LCP particles and MWCNTs (referred to as LCP-CNT-postmix) was fabricated by mixing bare LCP particles (99 wt. %) and MWCNTs (1 wt. %) together with the same contents of carbon black and PVdF binder as in the other cathodes. Coin cells were assembled with a cathode/LP30 electrolyte/Li metal anode with a 20-μm-thick monolayer polyethylene separator (Celgard K2045) in a 2016 coin cell case. The LP30 electrolyte, purchased from BASF, was composed of LiPF$_6$ salt dissolved in ethylene carbonate (EC) and dimethyl carbonate (DMC) (LiPF$_6$/EC/DMC = 11.8/44.1/44.1 wt. %). The inner surface of the cathode case was sputter-deposited with Au to prevent the oxidation of the stainless steel 304 case at high voltages.

2.3 Characterization

X-ray diffraction (XRD) analysis was performed to confirm the crystal structures of the CNTs, bare LCP particles, and LCP-CNT composite particles. XRD measurements were obtained using a Bruker D2 Phaser XRD with Cu K$_\alpha$ radiation (λ = 0.154 nm). The 2θ scanning range was 10 - 80°

at the scanning rate of ~0.0406°/s. After forming flat layers of particles on glass plates, CNTs, bare LCP, and LCP-CNT composite particles were measured by Raman spectroscopy (Renishaw) using a 514 nm Ar laser excitation source to investigate the effect of the embedded CNTs on the Raman peaks and confirm the co-existence of CNTs and LCP.

The sizes and shapes of particles and CNTs were observed by SEM (Oxford, 10 kV acceleration voltage). Cross-sectional images of the LCP-CNT composite particles were observed utilizing FIB-SEM (Scios^{TM}, FEI Company). Two Pt layers were consecutively deposited to protect the materials from the Ga ions. The first 200-nm-thick Pt layer was deposited by a 5 kV electron beam; the second 1.5-μm-thick Pt layer was formed by a 30 kV ion beam. Rough cuts and cleaning of the cross-section were performed by an ion beam with a current density of 5.0 nA at 30 kV. The fine milling process was performed with a current density of 0.5 nA at 30 kV as controlled by the software (Auto Slice and View G3, FEI Company). The thickness of each slice was 5 nm. LCP-CNT composite particles were also analyzed with transmission electron microscopy (TEM) (FEI Tecnai F20 G^2) operated at 200 kV in bright field high-resolution modes. Selected-area electron diffraction (SAED) patterns were also obtained to confirm the crystal structures during TEM observation.

2.4 Electrochemical measurements

The coin cells were charged and discharged in the voltage range of 3.0 - 5.1 V at a rate of 0.05 C with a battery tester (Arbin), with 1 C = 167 mAh/g, to evaluate the capacities of battery cells with different cathodes. CVs were obtained with a BioLogic potentiostat in the voltage range of 3.0 - 5.1 V with a sweep rate of 1 mV/s to compare the intercalation/de-intercalation voltages of Li$^+$ in the different cathodes. To analyze the impedance behaviors of the different coin cells, EIS were obtained with a BioLogic impedance analyzer in the open-circuit voltage (OCV) state after charging to 5.1 V by CV at a scanning rate of 1 mV/s.

3. RESULTS AND DISCUSSIONS

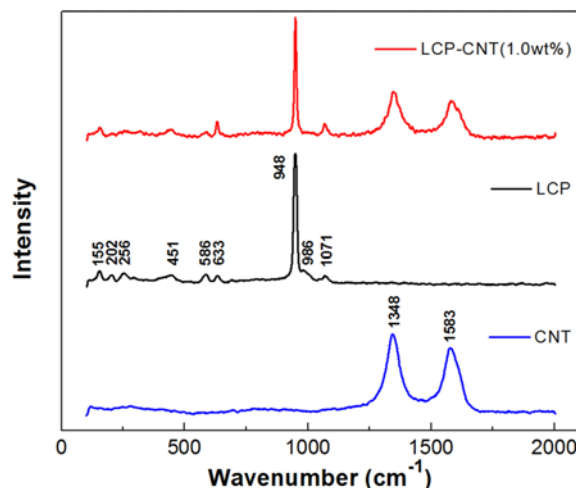### 3.1 Materials characterization

Figure 2 shows the XRD analysis results for the synthesized bare LCP particles, LCP-CNT composite particles, and MWCNTs. The pattern of MWCNTs shows two main peaks indexed to the (002) and (100) planes, which match well with the published crystal structure information on CNTs.[30,31] The patterns from the synthesized bare LCP particles exhibit main peaks indexed to the (101), (111), (201), (020), and (311) planes of orthorhombic LCP;[9] identical XRD peaks appear in the pattern obtained from the LCP-CNT composite particles. Other XRD peaks differing from those of the bare LCP particles are not observed in the pattern for the LCP-CNT composite particles, indicating that the embedded
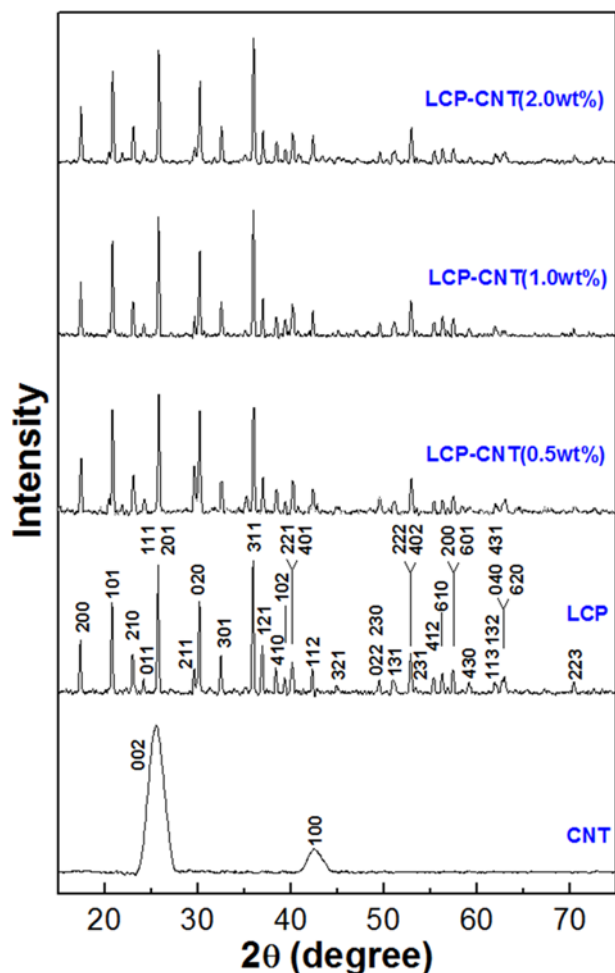
Fig. 2. XRD patterns of MWCNTs, bare LCP particles, and LCP-CNT composite particles with different MWCNT contents.

Fig. 3. Raman spectra of MWCNTs, bare LCP particles, and LCP-CNT composite particles.

MWCNTs do not significantly affect the crystal structure of LCP. In the XRD pattern of the LCP-CNT composite particles, peaks from the MWCNTs cannot be distinguished because the main peaks of MWCNTs and LCP overlap at $2\theta = \sim 26°$ and the amount of MWCNTs is relatively small compared to that of the LCP material. More detailed structural analysis for the bare and MWCNT-embedded LCP materials, for example, with higher quality XRD data, the Rietveld refinement analysis can be applied, which will provide more quantitative information on the crystal structure of materials. Such additional analysis is being pursued and the results will be reported in future publications.

Raman spectroscopy measurements for the MWCNTs, as seen in Fig. 3, show two main peaks at 1348 cm^{-1} and 1583 cm^{-1}, assigned to the D-band and G-band, respectively.[32-34] The synthesized bare LCP particles have a main Raman peak at 948 cm^{-1} attributed to symmetric vibrations of PO_4^{3-} anions.[35] The LCP-CNT composite particles exhibit the main Raman peaks of both LCP and MWCNTs,

as seen in Fig. 3, which demonstrates the co-existence of LCP and MWCNTs. Interestingly, the D-band and G-band of MWCNTs can be identified in the LCP-CNT composite particles by Raman spectroscopy, although XRD results do not clearly show the existence of MWCNTs in the LCP-CNT composite.

The MWCNTs used for this research are 10 - 30 nm in diameter and micron-scale in length, as shown in Fig. 4(a). The bare LCP particles and LCP-CNT composite particles range from 100 nm to 3 μm in size. The MWCNTs in the LCP-CNT composite particles (Fig. 4(c)-(e)) are distributed more uniformly than those in the LCP-CNT-postmix sample (Fig. 4(f)), in which MWCNTs are agglomerated and adhered to the surface of LCP particles, rather than embedded or implanted in the particles. Although MWCNTs have the high electrical conductivity of $10^2 - 10^5$ S/cm, they cannot contribute to the reduction of the electrical resistance of LCP particles when located on the surface of LCP particles. Therefore, the battery cell with the LCP-CNT composite particles is expected to achieve better performance in battery tests than those with bare LCP or LCP-CNT-postmix particles.

3.2 Carbon nanotube-embedded structure

TEM and FIB-SEM analyses were conducted to observe the embedded structures of MWCNTs and LCP-CNT composite particles. Figure 5(a) shows a LCP-CNT composite particle composed of many MWCNTs combined with the LCP particle, from which it can be assumed that MWCNTs are embedded within the LCP particles. A SAED pattern is obtained for the LCP-CNT composite particles during TEM observation, as shown in Fig. 5(b), and the d-spacing determined from the SAED pattern matches with the reported data of LCP.[9] MWCNTs have (002) and (100) plane d-spacings similar to LCP, which impedes the
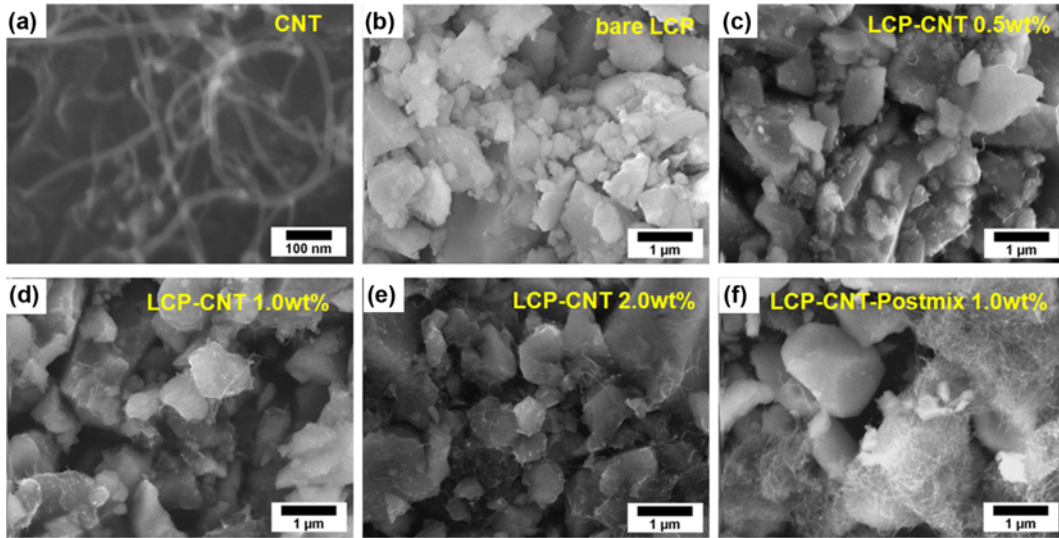
Fig. 4. SEM images of (a) MWCNTs, (b) synthesized bare LCP particles, LCP-CNT composite particles with (c) 0.5 wt. % MWCNTs, (d) 1.0 wt. % MWCNTs, (e) 2.0 wt. % MWCNTs, and (f) LCP-CNT-postmix particles.
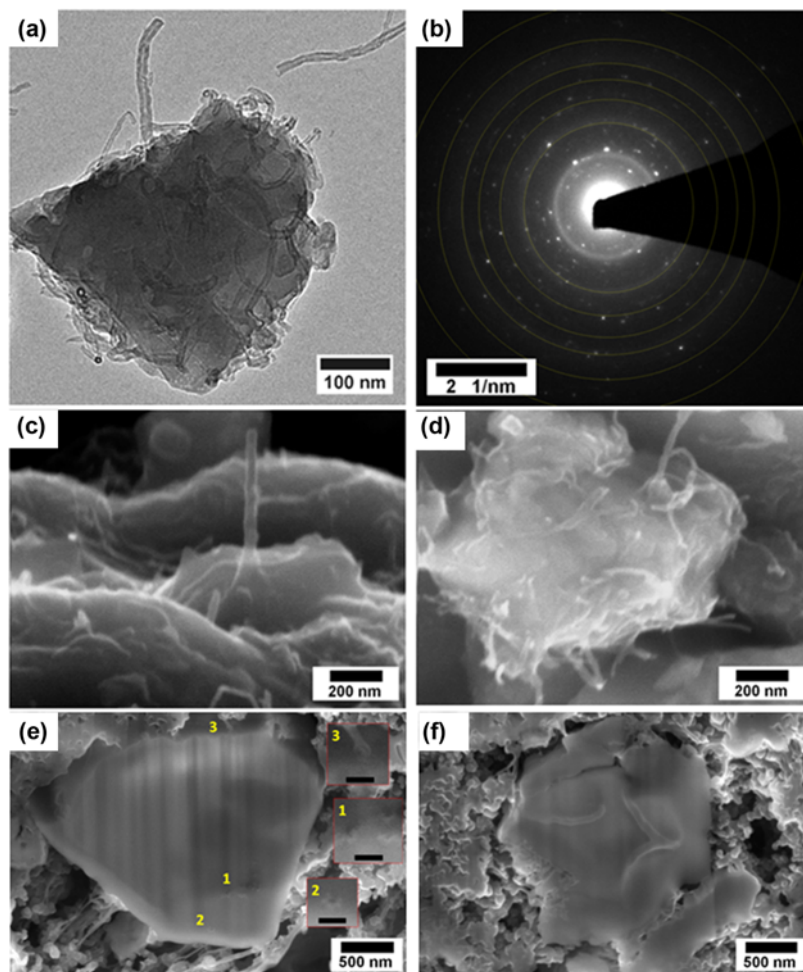
Fig. 5. (a) TEM image of LCP-CNT composite particle, (b) SAED pattern of LCP-CNT composite particles, (c) SEM image of MWCNT protruding from LCP surface, (d) SEM image of LCP-CNT composite particle, and FIB-SEM cross-sectional images showing (e) nano-holes (inset #1 and #2) and MWCNTs (inset #3) and (f) the trace of MWCNTs.

Table 1. d-spacing and crystal planes of LCP and CNTs, determined by SAED patterns in Fig. 5.

d-spacing (Å)	Crystal Plane of LCP	Crystal Plane of CNT
5.2	(200)	
4.2	(101)	
3.46	(111) (201)	(002)
3.0	(020) (301)	
2.5	(311)	
2.1	(112) (202)	(100)

identification of MWCNTs in SAED patterns, as listed in Table 1. Figure 5(c) shows one MWCNT protruding from the surface of a LCP particle and the cross-sectional image in Fig. 5(e) shows nano-holes (inset images #1 and #2) formed from MWCNTs sliced by FIB, as well as a MWCNT (inset image #3) protruding vertically from the LCP particle surface. These imply that MWCNTs are not simply adhered to the surface of LCP, but are instead embedded in the LCP particles. Some short MWCNTs are observed on the LCP particles surface in Fig. 5(a), (c), (d), and (e), which may be end portions of embedded MWCNTs protruding from the LCP particles. The embedded nature of the MWCNTs within LCP particles is expected to improve the electron mobility inside the LCP particle, which may eventually increase the electrical conductance of the LCP-CNT composite particle.

3.3 Charge-discharge capacity

Figure 6 displays the first cycle capacity in the charge-discharge tests of coin cells fabricated with bare LCP, LCP-CNT composite, and LCP-CNT-postmix cathodes. When considering discharge capacities observed at 4.25 V, the battery test results show discharging capacities of 24.4, 35.8, 52.5, 43.2, and 9.1 mAh/g in the cells of bare LCP particles, LCP-0.5 wt. % MWCNT composite, LCP-1.0 wt. % MWCNT composite, LCP-2.0 wt. % MWCNT composite, and LCP-CNT-postmix particles with 1.0 wt. % MWCNTs, respectively, as listed in Table 2.

All tested coin cells take much longer to charge than to discharge, which may result from the partial decomposition of the LP30 electrolyte at high voltages of ~5.0 V (vs. Li anode).[36] Therefore, only the first cycle behavior of the coin cells is evaluated to determine the optimal amount of MWCNTs in the LCP-CNT composite particles and to compare the capacity of cells with LCP-CNT composite
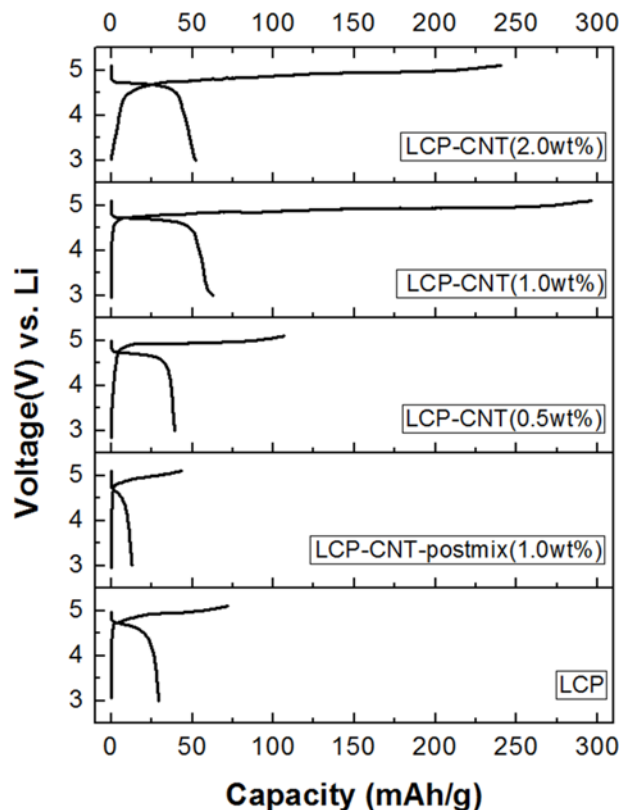
Fig. 6. The first-cycle cell capacity in charge-discharge tests of coin cells fabricated with bare LCP, LCP-CNT-postmix, and LCP-CNT composite cathodes.

cathodes to that of the cell containing the LCP-CNT-postmix cathode.

Based on the discharge capacities shown in Fig. 6, the optimal amount of MWCNTs is 1.0 wt. %; the capacity gradually increases and reaches a maximum value of 52.5 mAh/g as the amount of MWCNTs increases from 0 to 1.0 wt. %, but the capacity decreases with further addition of MWCNTs. The main effects contributing to this capacity behavior are analyzed by CV and EIS. The relationships correlating capacity, conductance, and the amount of MWCNTs are now discussed.

3.4 MWCNT-embedding effect on redox potentials

When a material with a dissimilar reaction potential is added to a cathode material, it can change the electrochemical redox potentials and eventually affect the cell performance. To observe the effect of the embedding of MWCNTs within

Table 2. Charge-transfer resistance R_{ct} and discharge capacity of coin cells with different cathodes.

	LCP (bare)	LCP-CNT (0.5 wt. %)	LCP-CNT (1.0 wt. %)	LCP-CNT (2.0 wt. %)	LCP-CNT (1.0 wt. %)
Rct (Ω)	150	110	80	65	170
Disch. Capacity at 4.25 V(mAh/g)	24.4	35.8	52.5	43.2	9.1
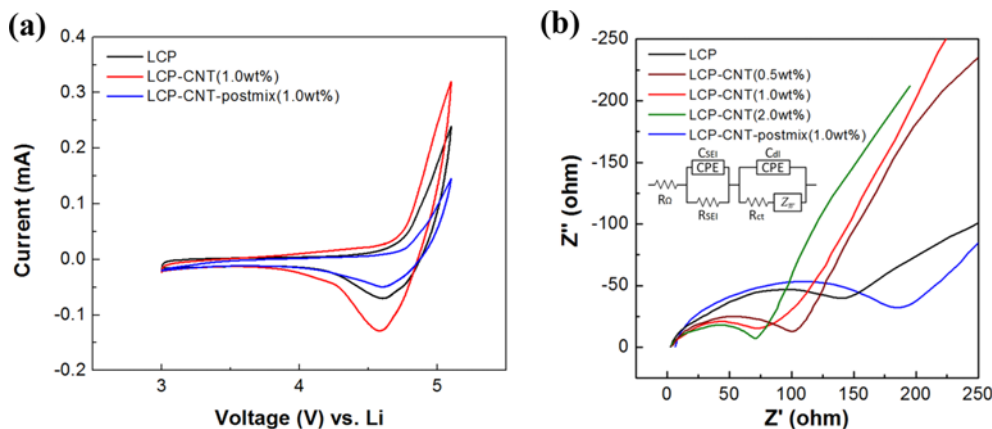
Fig. 7. (a) Cyclic voltammograms of coin cells with bare LCP, LCP-CNT composite, and LCP-CNT-postmix cathodes. (b) EIS results for coin cells with bare LCP, LCP-CNT composites, and LCP-CNT-postmix cathodes. Inset: circuit model for coin cells (R_Ω: ohmic resistance, *CPE*: constant phase element, C_{SEI}: capacitance by SEI layer, R_{SEI}: resistance by SEI layer, C_{dl}: electrical double-layer capacitance, R_{ct}: charge-transfer resistance, Z_w: Warburg impedance).

LCP particles on the charge-discharge voltages, CV is performed for cells with bare LCP particles, LCP-CNT composite particles, and LCP-CNT-postmix particles at a scanning rate of 1 mV/s. Figure 7(a) shows that the peak voltages of the discharge reaction by the intercalation of Li⁺ into the cathode range from 4.59 - 4.61 V for the cells with different cathodes. The cell with the LCP-CNT composite cathode has a discharge peak voltage ~20 mV lower than those of cells with bare LCP and LCP-CNT-postmix cathodes. The embedded MWCNTs may contribute to this small decrease in discharge voltage since the MWCNTs have an lithiation voltage below 1.0 V (vs. Li/Li⁺).[12] Additional work is necessary to correctly interpret the voltage behavior of the LCP-CNT composite cathode. The cell with the LCP-CNT-postmix cathode has a discharging voltage similar to that of the bare LCP cathode, indicating that the MWCNTs in the mixed cathode are not embedded in the LCP particles. The charging voltages for the de-intercalation of Li⁺ from the cathodes for all cathodes do not show current peak maxima but instead increase gradually up to 5.1 V, which may result from the aforementioned partial decomposition of the LP30 electrolyte. CNTs can also be intercalated with Li⁺ below 1.0 V (vs. Li).[12] However, the voltage of the current battery tests ranges from 3.0 to 5.1 V, which prohibits Li⁺ intercalation into MWCNTs in the LCP-CNT composite particles. Therefore, the intrinsic capacity of MWCNTs does not significantly affect the total discharge capacity of the LCP-CNT composite cathodes.

3.5 MWCNTs-embedding effect on impedance

To measure the charge-transfer resistance (R_{ct}) for the Li⁺ intercalation/deintercalation reaction, electrochemical impedance spectroscopy (EIS) is performed on coin cells with bare LCP, LCP-CNT composite, and LCP-CNT-postmix cathodes. Figure 7 shows the impedance measurement results, in which semi-circles occur in the high- to low-frequency range of 1 MHz to 50 - 100 Hz. The spectra are composed of one small semi-circle in the high-frequency range and a second large semi-circle in the low-frequency range, which can be distinguished with much care and is more apparent in the black-colored graph of bare LCP in Fig. 7(b). The first intercept in the Z'-axis represents the ohmic resistance, mainly affected by the electrolyte. A small semi-circle at high frequency is regarded as the impedance formed by solid-electrolyte interface (SEI) layer, and a large semi-circle at low frequency is assigned to the impedance generated by R_{ct} and electrical double-layer capacitance. The linear increase of impedance after the semi-circles is caused by Li⁺ diffusion inside particles, referred to as the Warburg impedance.[37] Based on this interpretation, an equivalent circuit model is shown in the inset of Fig. 7(b), similar to typical models in reported results. As shown in Table 2 and Fig. 7(b), R_{ct} is decreased gradually from ~150 to ~65 Ω as the amount of embedded MWCNTs is increased from 0.0 to 2.0 wt. % in the LCP-CNT composite cathodes. However, the coin cell with the LCP-CNT-postmix cathode has a high R_{ct} of ~170 Ω, despite the 1.0 wt. % of MWCNTs. This high R_{ct} value may result from the non-contribution of MWCNTS to electron mobility within the LCP particles, because the MWCNTs are only located on the surfaces of the LCP particles in the mixture.

3.6 Main factors affecting the cell capacity behavior

As shown in Fig. 8, the R_{ct} can be transformed to the conductance for the intercalation/de-intercalation reaction by: Conductance [S] = Resistance⁻¹ [Ω⁻¹]. The discharge capacity increases proportionally with the conductance up to 1.0 wt. % of MWCNTs in the LCP-CNT composite cathodes.
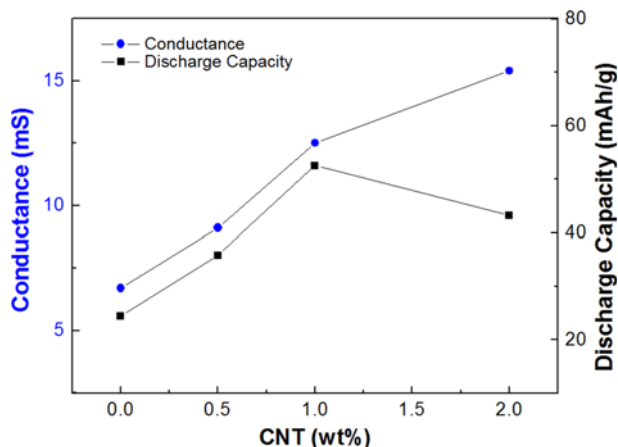
Fig. 8. Relation between MWCNT levels and conductance and discharge capacity of cells fabricated with bare LCP and LCP-CNT composite cathodes.

Interestingly, the discharge capacity then decreases inversely with conductance for the LCP-CNT composite cathode with 2.0 wt. % MWCNTs. The higher conductance of the LCP-CNT composite cathodes may be a primary factor affecting the cell capacity, because the LCP-CNT composite cathodes have smaller R_{ct} values compared to the bare LCP cathode. The uniformity of MWCNT distribution in LCP-CNT composite particles may also affect the cell capacity. In the LCP-CNT composite particles, MWCNTs at 2.0 wt. % cannot be dispersed uniformly during the gelation step of LCP synthesis. This may induce MWCNT agglomeration, which may isolate some regions of LCP from the electrolyte and lower the Li^+ diffusivity between the LCP and electrolyte.

4. CONCLUSIONS

MWCNT-embedded LCP particles (LCP-CNT composite particles) were fabricated by dispersing MWCNTs during the gelation step of LCP synthesis, by which uniform distributions of MWCNTs were achieved within LCP particles as observed by TEM and FIB-SEM analysis. The olivine crystal structure of the synthesized LCP-CNT composite particles was confirmed by XRD analysis. Raman spectroscopy analysis demonstrated the co-existence of MWCNTs with LCP. The LCP-CNT composite cathode showed much better performance than the bare LCP cathode and the LCP-CNT-postmix cathode. The optimal amount of MWCNTs is 1.0 wt. % based on the first-cycle discharging capacity. The main factors contributing to the increased cell capacity are the reduced charge transfer resistance observed by EIS and the uniform dispersion of MWCNTs.

ACKNOWLEDGEMENT

REFERENCES

1. B. Dunn, H. Kamath, and J.-M. Tarascon, *Science* **334**, 928 (2011).
2. M. M. Thackeray, C. Wolverton, and E. D. Isaacs, *Energy Environ. Sci.* **5**, 7854 (2012).
3. D. Howell, *Fiscal Year 2012 Annual Progress Report for Energy Storage R&D*, p. 1-8, US Department of Energy's EERE, DOE/EE-0844 (2013).
4. H.-A Choi, H. Jang, H. Hwang, M. Choi, D. Lim, S. E. Shim, and S.-H. Baeck, *Electron. Mater. Lett.* **10**, 957 (2014).
5. C. Guille and G. Gross, *Energy Policy* **37**, 4379 (2009).
6. H. Ibrahim, A. Ilinca, and J. Perron, *Renewable Sustainable Energy Rev.* **12**, 1221 (2008).
7. V. Aravindan, J. Gnanaraj, Y.-S. Lee, and S. Madhav, *J. Mater. Chem.* **A 1**, 3518 (2013).
8. A. Manthiram, *J. Phys. Chem. Lett.* **2**, 176 (2011).
9. F. Kubel, *Z. Kristallogr.* **209**, 755 (1994).
10. F. Yu, L. Zhang, M. Zhu, Y. An, L. Xia, X. Wang, and B. Dai, *Nano Energy* **3**, 64 (2014).
11. Z. Gong and Y. Yang, *Energy Environ. Sci.* **4**, 3223 (2011).
12. B. J. Landi, M. J. Ganter, C. D. Cress, R. A. DiLeo, and R. P. Raffaelle, *Energy Environ. Sci.* **2**, 638 (2009).
13. G. Hautier, A. Jain, S. P. Ong, B. Kang, C. Moore, R. Doe, and G. Ceder, *Chem. Mater.* **23**, 3495 (2011).
14. L.-X. Zhang, Y.-Z. Wang, H.-F. Jiu, Y.-L. Wang, Y.-X. Sun, and Z. Li, *Electron. Mater. Lett.* **10**, 439 (2014).
15. K. Zaghib, A. Mauger, J. B. Goodenough, F. Gendron, and C. M. Julien, *Chem. Mater.* **19**, 3740 (2007).
16. P. S. Herle, B. Ellis, N. Coombs, and L. F. Nazar, *Nat. Mater.* **3**, 147 (2004).
17. J. Wolfenstine, *J. Power Sources* **158**, 1431 (2006).
18. H. Tukamoto and A. R. West, *J. Electrochem. Soc.* **144**, 3164 (1997).
19. F. Zhou, K. Kang, T. Maxisch, G. Ceder, and D. Morgan, *Solid State Comm.* **132**, 181 (2004).
20. C. Ling, D. Banerjee, W. Song, M. Zhang, and M. Matsui, *J. Mater. Chem.* **22**, 13517 (2012).
21. J. van Elp, J. L. Wieland, H. Eskes, P. Kuiper, and G. A. Sawatzky, *Phys. Rev. B: Condens. Matter Mater. Phys.* **44**, 6090 (1991).
22. R. H. Baughman, A. A. Zakhidov, and W. A. de Heer, *Science* **297**, 787 (2002).
23. T. W. Odom, J.-L. Huang, P. Kim, and C. M. Lieber, *Nature* **391**, 62 (1998).
24. S. Frank, P. Poncharal, Z. L. Wang, and W. A. de Heer, *Science* **280**, 1744 (1998).
25. B. Marinho, M. Ghislandi, E. Tkalya, C. E. Koning, and G. de With, *Powder Technol.* **221**, 351 (2012).
26. T. W. Ebbesen, H. J. Lezec, H. Hiura, J. W. Bennett, H. F. Ghaemi, and T. Thio, *Nature* **382**, 54 (1996).

27. Q. D. Truong, M. K. Devaraju, Y. Ganbe, T. Tomai, and I. Honma, *Sci. Rep.* DOI: 10.1038/srep03975 (2014)
28. J. Ni, H. Wang, L. Gao, and L. Lu, *Electrochim. Acta* **70**, 349 (2012).
29. L. Dimesso, C. Spanheimer, W. Jaegermann, Y. Zhangb, and A. L. Yarin, *Electrochim. Acta* **95**, 38 (2013).
30. T. M. Keller, S. B. Qadri, and C. A. Little, *J. Mater. Chem.* **14**, 3063 (2004).
31. F. Wang, J. Yang, Y. NuLi, and J. Wang, *J. Power Sources* **196**, 4806 (2011).
32. F. Tuinstra and J. L. Koenig, *J. Chem. Phys.* **53**, 1126 (1970).
33. M. S. Dresselhaus, G. Dresselhaus, R. Saito, and A. Jorio, *Phys. Rep.* **409**, 47 (2005).
34. N. Yan, X. Zhou, Y. Li, F. Wang, H. Zhong, H. Wang, and Q. Chen, *Sci. Rep.* DOI: 10.1038/srep03392 (2013).
35. E. Markevich, R. Sharabi, O. Haik, V. Borgel, G. Salitra, D. Aurbach, G. Semrau, M. A. Schmidt, N. Schall, and C. Stinner, *J. Power Sources* **196**, 6433 (2011).
36. S. M. G. Yang, V. Aravindan, W. I. Cho, D. R. Chang, H. S. Kim, and Y. S. Lee, *J. Electrochem. Soc.* **159**, A1013 (2012).
37. H.-M. Cho, W.-S. Choi, J.-Y. Go, S.-E. Bae, and H.-C. Shin, *J. Power Sources* **198**, 273 (2012).